CrystEngComm

Accepted Manuscript

ROYAL SOCIETY OF CHEMISTRY

www.rsc.org/crystengcomm

Morphological evolutions and growth patterns of Zr–containing phases in aluminum alloys

Tong Gao, Xiaoli Cui, Xiongying Li, Hui Li, Xiangfa Liu*

Key Laboratory for Liquid–Solid Structural Evolution and Processing of Materials, Ministry of Education, Shandong University, 17923 Jingshi Road, Jinan 250061, PR China

* Corresponding author. Tel.: +86 531 88392006; fax: +86 531 88395414.

E–mail address: xfliu@sdu.edu.cn (Xiangfa Liu).

Abstract:

Three–dimensional morphologies of Zr–containing phases in Al–(Si–)Zr alloys were studied in detail using field emission scanning electron microscopy. Combining the analysis of crystallographic features with atomic arrangements in the crystal lattices and first–principles quantum mechanics calculations, the growth mechanisms of Zr–containing phases were discussed. As reported in previous work, the increase of Si content in Al–(Si–)Zr alloys leads to the continuous composition evolution and a structure transformation from $ZrAl_3$ to (Al,Zr,Si) and $ZrSi_2$. The perfect morphology of $ZrAl_3$ is compressed cubic, whose lateral surfaces are composed of four groups of symmetric planes. (Al,Zr,Si) has similar crystal shape with $ZrAl_3$, while the cube is much thicker and the growth process is changed. The further high Si content results in the formation of $ZrSi_2$ phase, presenting eighteen polyhedral morphology, whose upper and lower surfaces are also covered by (0 0 1) planes, while its lateral surface composes of eight groups of symmetric {1 1 0} and {1 1 1} planes. Similar growth mechanisms of Ti–containing phases in Al–(Si–)Ti alloys have also been found.

Keywords: Zr–containing intermetallics; Microstructure; Morphology; Crystal growth

1. Introduction

Al–Si alloys are well–known casting alloys and widely used in many fields, due to the low thermal–expansion coefficient, high wear resistance and improved mechanical properties [1–3]. The attempt to improve mechanical properties of Al–Si alloys by alloying has been widely investigated, and it is known that the addition of transition metals, *e.g.* Sc, Ti and Zr, will lead to the formation of intermetallic compounds [4–7]. Take element Zr as an example, there may exist several kinds of phases with different morphologies depending on the casting parameters in Al–Si–Zr alloys [8, 9]. In our previous work, we have also done some research on the composition and structural evolutions of Ti–containing and Zr–containing phases [10, 11]. With the increase of Si content from 0 to 60% (all compositions quoted in this work are in wt.% unless otherwise stated) in Al–xSi–2Zr alloys, the Zr–containing phase was detected to evolve from $ZrAl_3$ to (Al,Zr,Si) and then $ZrSi_2$. Also, due to the replacement effect between Al and Si atoms in the crystal lattices, the composition of each phase can also vary over a wide range [12–14]. Therefore, no constant stoichiometric formula can be accurately defined to represent for the Zr–containing phases, thus, ZrAlSi is commonly used for short, just as TiAlSi is used to mark Ti–containing phases [7, 11].

ZrAlSi, TiAlSi or other intermetallics containing transition metal elements are quite important in aluminum alloys. For instance, Zr–containing phase can keep stable at relatively high temperature and is regarded as a promising candidate to enhance the elevated–temperature properties of Al–Si alloys [7]. Precipitation of Ti–containing phase leads to an increase of microhardness of the alloys [6]. However, so far, the application of ZrAlSi or TiAlSi intermetallics is quite limited, due to the rare technology controlling its distribution and morphology.

According to various references, TiAlSi and ZrAlSi phases can exhibit several morphologies,

i.e. blocky, flake–like and petal–like, which may be determined by element content and cooling rate [6, 15, 16]. Commonly, most of the TiAlSi and ZrAlSi particles reported in either the references or our previous work are flake–like [6, 7, 10, 11]. During our further investigation of Al–Si–Zr system, blocky ZrAlSi particles are obtained, which exhibit obvious geometrical outlines, indicating that the crystals expose faceted planes and crystallographic features [17]. The crystal characteristic of $ZrAl_3$ has been determined by S. Zhen *et al.* [18] and L. Lei *et al.* [19], and the fully grown primary $ZrAl_3$ crystals are tabular and bound by {0 0 1} and {1 0 1} facets. However, the identification is mostly based on two–dimensional observation, and some deviation is also unavoidable.

As is known, crystal growth is a stage following the nucleation, which is of practical interest as it is intimately related to the macro– and micro–structures and hence the properties of the materials. The purpose to write this paper is to provide direct crystallographic information for the possible formed Zr–containing phases, *i.e.* $ZrAl_3$, (Al,Zr,Si) and $ZrSi_2$, as mentioned above in Al–xSi–Zr alloys. Using special method, the three–dimensional morphologies of the crystals can be observed directly. Besides, rapid solidification method can be applied to keep the initial growth form of crystals. We hope this part of work can contribute to the complete understand of Al–Si–Zr alloys, combining with previous literatures.

2. Experimental

The materials used in this paper are commercial purity Al (99.7%), commercial pure crystalline Si (99.9%) and K_2ZrF_6 salt (99 %). According to the previous experience, the content of Si in the melt plays an importance role in the evolution of ZrAlSi phase. Thus, Al–5Zr, Al–10Si–5Zr and Al–25Si–5Zr alloys were prepared to obtain $ZrAl_3$, (Al,Zr,Si) and $ZrSi_2$ phases,

respectively. The process is as follows: Al ingots were firstly melting in a clean clay–bonded graphite crucible heated by 25kW medium frequency induction furnace to 780 ℃, and then Si bulks were added in the melt. After the melt was heated up to 800 ℃, K_2ZrF_6 salt was gradually added in the melt. Due to the reduction reaction between Al, Si atoms and K_2ZrF_6, element Zr was absorbed, resulting in the formation of ZrAlSi phases, while $KAlF_4$ and K_3AlF_6 liquids were floated on aluminum melt. After pouring the above liquids and cleaning the dregs, the melt was poured into a cast iron chill.

Metallographic specimens were all cut from the same position of the as–cast samples, then mechanically ground and polished in standard routines. The microstructure analysis was carried out by field emission scanning electron microscopy (FESEM). The investigation was applied using a SU–70 scanning electron microscope operated at 15KV and linked with an energy dispersive spectrometry (EDS) attachment. Some images were captured by observing the deep etched samples or fractograph of the alloys. XRD measurements of the polished samples were conducted in a Rigaku D/max–rB diffractometer using Cu–Kα radiation at 40KV and 100mA.

In order to observe three–dimensional morphologies of the particles in the prepared alloys, the aluminum matrix was dissolved in a solution with 10 vol.% of HCl or NaOH. The extracted sediments were collected using a centrifugal extractor (TGL–16C), and then rinsed with distilled water and ethanol. After drying, the sediments were also analyzed by FESEM.

Besides, first–principles quantum mechanics calculations were conducted to indicate the surface energy of crystal faces by using a state–of–the–art quantum mechanics–based program (CASTEP) in Materials Studio package. CASTEP employs the density functional theory (DFT) plane–wave pseudopotential method, which performs first–principles quantum mechanics calculations that

explore the properties of crystals and surfaces in materials [20, 21]. The atomic interactions were treated with the projected augmented wave (PAW) pseudopotentials, using the Perdew Burke Ernzerhof (PBE) exchange–correlation functional for the spin–polarized generalized gradient correction with the plane–wave energy cutoff of 270 eV and 1×1×1 k–point mesh. The surface energy is characterized by the equation:

$$E = \left(E_{slab} - E_{bulk}\right)/2 \qquad (1)$$

where E_{slab} is the total energy of the crystal with certain faces exposed to vacuum with a thickness of 10 Å, E_{bulk} is the total energy of bulk crystals.

3. Results and discussion

3.1 XRD identification and crystal structures of ZrAlSi

As mentioned above, in our previous work, we found that the ZrAlSi phase forms as $ZrAl_3$ in binary Al–Zr alloy, (Al,Zr,Si) in ternary Al–xSi–Zr alloys when Si content is low (*e.g.* 10 wt.%), and $ZrSi_2$ when Si content is high (*e.g.* 25 wt.%). In this paper, three typical Al–5Zr, Al–10Si–5Zr and Al–25Si–5Zr alloys were prepared, and the corresponding XRD patterns are shown in Fig. 1. As marked on the diffraction peaks, $ZrAl_3$, (Al,Zr,Si) and $ZrSi_2$ phases were obtained, respectively. According to various references, (Al,Zr,Si) phase may also be marked as τ_1, $(Al,Si)_3Zr$ or $Zr(Al_{1-x}Si_x)_3$. Since the Si atoms in $ZrSi_2$ crystal lattice can be replaced by Al atoms to some extent, for instance, as high as 7.27 at.% Al can be detected in $ZrSi_2$ phase in Al-18Si-2Zr alloy [11],thus, the chemical formula $Zr(Si_{1-x}Al_x)_2$ is commonly used to clearly indicate the composition variance, which still keeps the crystal structure of $ZrSi_2$. However, it is necessary to mention that even though some scientists simply marked (Al,Zr,Si) as $Zr(Al_{1-x}Si_x)_3$, meaning that some Si atoms occupy the sites of Al atoms in the crystal lattice of $ZrAl_3$, the diffraction peaks of (Al,Zr,Si)

are quite different from those of $ZrAl_3$ phase, as shown in Fig. 1a and b. Fig. 2 presents the crystal structure and the atomic arrangement on <0 0 1> and <1 0 0> faces. It can be found that $ZrAl_3$ belongs to tetragonal system, presenting a $D0_{23}$ structure (a=0.4013nm, c=1.7321nm) [22], as shown in Fig. 2a. However, with the participation of Si in $ZrAl_3$, the (Al,Zr,Si) phase belongs to the tetragonal system, while it presents a $D0_{22}$ structure (a=0.392nm, c=0.894nm) [23]. As a result, the diffraction peaks of $ZrAl_3$ and (Al,Zr,Si) phases are quite different, due to the difference of lattice parameters. Take a good look at the diffraction peaks of $ZrSi_2$ phase (Fig. 1c) and the crystal structure (Fig. 2c), it can be identified that the phase belongs to orthorhombic system, with the lattice parameters a=0.372nm, b=1.461nm and c=0.367nm, respectively [24]. The doping of Al in $ZrSi_2$ leads to a shift of diffraction peaks. For instance, the interplanar spacing values of (1 1 1) and (0 0 2) faces shift from standard 2.5700 μm and 1.8300 μm to 2.5783μm and 1.8376μm, by comparing the values in PDF data base with those shown in Fig. 1c.

In our further study, $ZrAl_3$, (Al,Zr,Si) and $ZrSi_2$ particles were extracted from the aluminum matrix. Their morphologies and three–dimensional shapes were observed directly using FESEM. It was found that these ZrAlSi phases have obvious crystallographic features. Generally speaking, the intrinsic crystal structure is the fundamental factor that determines the final habit and morphology of a crystal [25, 26]. The intrinsic factors are prone to lead to the equilibrium crystal shape with minimum total surface energy. In the following section, the morphologies and growth mechanisms of $ZrAl_3$, (Al,Zr,Si) and $ZrSi_2$ were discussed, respectively.

3.2 Growth mechanisms of ZrAlSi

3.2.1 Morphology and growth mechanism of $ZrAl_3$

Fig. 3a–b shows the microstructure of Al–5Zr master alloy and typical three–dimensional

morphology of $ZrAl_3$ crystal. It can be seen that most of the particles exhibit regular blocky or rod–like shape in the polished sample (Fig. 3a). The extractive crystals show compressed cubic morphologies (Fig. 3b), and the thickness of the crystal is quite small. Most of the particles have the size ranging from 1 to 10 μm. Besides, it seems that the lateral surfaces are composed of four groups of symmetric inclined planes. Fig. 3c is the corresponding EDS result, which displays the composition of $ZrAl_3$.

Bravais first derived an empirical rule that crystal faces parallel to the net planes with higher reticular densities (wider interplanar distances) develop larger on actual crystal than those with lower reticular densities [27]. Another approach to understand the polyhedral form of a crystal is thermodynamic analysis of the equilibrium form, discussed by J. W. Gibbs [28], P. Curie [29], G. Wulff [30]. Basically, they considered that a crystal is bounded by a combination of crystal faces whose total surface area and surface free energies are minimum. Hereafter, according to the crystallographic theory, the reticular densities are often calculated by many researchers to determine the possible surfaces, since high reticular density means less opportunity for atoms stacking, leading to a lower growth rate [31–33].

The atomic distribution of (0 0 1) (1 1 0) and (1 1 1) faces are displayed in Fig. 4a–c. Both the side view of the faces and the corresponding projection of atomic arrangements are performed clearly. It can be seen that the (0 0 1) face has the highest density, indicating it as the close–packed face. Compared with the (0 0 1) and (1 1 0) planes, (1 1 1) has the lowest reticular density. In the view of the attachment energy for new atoms at faces in $ZrAl_3$ crystal, atoms prefer to pack on the (1 1 1) face with high binding energy [34, 35]. That is to say, the (1 1 1) face has the highest growth rate along <1 1 1>, then (1 1 0) and (0 0 1).

To confirm this judgment, a program based on first–principles mechanics has been applied to calculate the surface energy of $ZrAl_3$ crystal. A total number of 64 atoms (48 Al atoms plus 16 Zr atoms) were chosen to build the model, then vacuum slabs were inserted among (0 0 1), (1 1 0) and (1 1 1) planes, respectively. Fig. 5 shows the calculated energy values of the model before and after inserting vacuum slabs. Conducted by the above equation (1), the surface energies of (0 0 1), (1 1 0) and (1 1 1) surfaces can be determined, *i.e.* 6.215 eV, 8.622 eV and 11.247 eV. It shows that the value of (0 0 1) is the lowest, compared with that of (1 1 0) and (1 1 1). Lower surface energy means that the surface is more stable, with a higher tendency to expose outside. On the contrary, the (1 1 1) surface with highest surface energy is prone to disappear, due to the fast growth rate along <1 1 1> direction. Thus, the calculation results are also consistent with the above judgment according to the atomic arrangements, as shown in Fig. 4.

Fig. 6a–d shows the typical morphologies of different growth stages of $ZrAl_3$ phase and the schematic image. It can be seen that at the initial stage, the $ZrAl_3$ particle exhibits flat polyhedron, whose side faces are covered by eight groups of {1 1 0} and {1 1 1} faces [19]. During the growth stage, the growth rate along <1 1 1> is the highest as discussed above. According to geometrical dimension, when the growth rate along <1 1 1> ($V_{\{1\,1\,1\}}$) is greater than $\sqrt{2}\ V_{<1\,1\,0>}$, the {1 1 1} planes will finally disappear. As a result, the equilibrium shape of $ZrAl_3$ develops to compressed cubic morphology.

3.2.2 Morphology and growth mechanism of (Al,Zr,Si)

As discussed above, the diffusion of Si into $ZrAl_3$ can result in the formation of ternary (Al,Zr,Si) phase. Fig. 7a–b shows the microstructure of the as cast Al–10Si–5Zr alloy and the morphology of fractograph. Compared the solidification microstructure with that of Al–5Zr alloy,

the introduction of Si leads to the precipitation of blocky particles, mostly exhibiting round or polygonal (Fig. 7a). From the three–dimensional morphology (Fig. 7b), we can see that the crystal has somewhat kept the characteristic of $ZrAl_3$, *i.e.* the whole crystal presents cubic, with symmetric angled planes covering the lateral surfaces. The difference is that the cubic is much thicker than that of $ZrAl_3$, and four planes perpendicular to the upper and lower surfaces appear, which looks like that a cut is applied at each corner of the upper surface. Also, the size of the particles is over a wide range, with the average value of about 15 μm (Fig. 7a). Fig. 7c shows the corresponding EDS result of the particle in Fig. 7b, which has the composition of 58.77 at.% Al, 13.05 at.% Si and 28.18 at.% Zr, confirming the chemical formula $Zr(Al_{1-x}Si_x)_3$.

As discussed above, the introduction of Si in $ZrAl_3$ has changed the crystal structure, and the atomic arrangements are quite different from those in $ZrAl_3$. Thus, the atomic distributions of the most close–packed faces were re–calculated, as displayed in Fig. 8, in which we simplify present Zr and Al atoms. It can be seen that the order of decreasing reticular densities is (0 0 1), (1 1 0), (0 1 1) and (1 1 1). This may indicate that the {1 1 1} crystal faces are quite easy to disappear during the growth stage. It is necessary to state that since the (Al,Zr,Si) phase has a relatively bad symmetric $D0_{22}$ structure, the arrangement of atoms on (1 1 0) or (1 0 1) planes are different from that on (0 1 1), even though they all belong to {1 1 0} family.

To clarify the growth process of the (Al,Zr,Si) crystal, several shapes were obtained during the growth process. Fig. 9 a–d shows the typical morphologies of (Al,Zr,Si) at different growth stages. Many researchers have pointed out that there exists microsegregation in the melt, and such microsegregation is beneficial for the formation of seed crystal at during solidification [33, 36]. The initial growth of the seed is diffusion controlled, and the radial growth rates in every direction

are isotropic, resulting in the formation of spherical (Al,Zr,Si) seed crystal (Fig. 9a). After further growth, the seed crystal begins to perform crystallographic features and the exposed faces are special crystal planes. According to the above calculations of atomic arrangements (Fig. 8), comparing with the crystallographic feature of $ZrAl_3$, by means of the geometrical orientation relationship between each plane, the crystal faces of the (Al,Zr,Si) can be identified.

Take the early growing stage crystal for example, as shown in Fig. 9e, the upper and lower surfaces are (0 0 1) and (0 0 $\bar{1}$) faces. Considering the geometrical positions, the lateral surfaces are (1 0 1), (1 0 $\bar{1}$), (0 1 1), (0 1 $\bar{1}$), ($\bar{1}$ 0 1), ($\bar{1}$ 0 $\bar{1}$), (0 $\bar{1}$ 1) and (0 $\bar{1}$ $\bar{1}$), respectively, just as the condition in $ZrAl_3$ crystal. Accordingly, the four perpendicular surfaces are (1 1 0), (1 $\bar{1}$ 0), ($\bar{1}$ 1 0) and ($\bar{1}$ $\bar{1}$ 0). With developing of the crystal (Fig. 9e–h), the growth of lateral surfaces results in the shrink of perpendicular planes. Finally, the crystal develops to a cube, whose lateral surfaces are covered by four groups of oblique {1 0 1} planes, as shown in Fig. 9d and h. However, comparing the morphology of (Al,Zr,Si) with $ZrAl_3$, the crystal of (Al,Zr,Si) is much thicker, which may indicate the faster growth rate along <0 0 1> direction.

Make a detailed morphological compare between $ZrAl_3$ and (Al,Zr,Si) crystals, it is obvious to find that there are some similarities. For instance, the final shapes of them are both cubic. However, the growth mechanisms of lateral surfaces are different, since the reticular densities of important planes in $ZrAl_3$ and (Al,Zr,Si) lattices are various, even though they both belong to tetragonal system.

3.2.3 Morphology and growth mechanism of $ZrSi_2$ phase

Another ZrAlSi phase has been mentioned above, *i.e.* $ZrSi_2$, which can be obtained in the melt with high Si concentration. The microstructure of Al–25Si–5Zr alloy and the morphology of $ZrSi_2$

are shown in Fig. 10a–c. It can be seen that amounts of blocky particles are synthesized in the alloy, exhibiting various polygonal outlines according to random cutting angles, as shown in Fig. 10a–b. From Fig. 10c, we can see the three–dimensional morphology of $ZrSi_2$ particles, which present polyhedral shapes, with obvious crystallographic features. The upper and lower surfaces of the crystal are two octagonal planes, and the laterals are covered by eight groups of oblique planes, just as those mentioned above in $ZrAl_3$ and (Al,Zr,Si) crystals. The word 18–polyhedron is used hereafter to describe this crystal. Fig. 10d displays the EDS result of the particle, and it has the composition of 7.20 at.% Al, 56.68 at.% Si and 36.12 at.% Zr, indicating the chemical formula $Zr(Si_{1-x}Al_x)_2$ as mentioned above.

Fig. 11 shows the morphologies of $ZrSi_2$ and scheme of the growth pattern. It clearly displays the three–dimensional 18–polyhedron morphology of this crystal. Here, we can look back at the initial crystal shape of $ZrAl_3$. As marked in Fig. 11d, eight groups of oblique planes are also found at the growth stage, while only four groups of planes are kept in the final $ZrAl_3$ crystal. Different from the competition result between {1 1 1} and {1 1 0} planes in $ZrAl_3$, the eight groups of planes are all retained in the final $ZrSi_2$ crystal. Also, the growth rate along <0 0 1> direction is also accelerated, and finally the crystal performs much thicker, as shown in Fig. 11b, c and e.

Based on the theory above, the atomic distributions of {1 1 0} and {1 1 1} planes of $ZrSi_2$ crystal were also calculated, as shown in Fig. 12. It can be found that the atomic density between {1 1 0} and {1 1 1} is quite similar, thus, they have similar growth rates. This information about atomic arrangement confirms the growth mechanism mentioned above. Besides, the surface energies of related planes have been calculated using first–principles quantum mechanics. The values of (1 1 0) and (1 1 1) faces in a 48 atoms (32 Si atoms plus 16 Zr atoms) model are

determined as 14.456 eV and 14.598 eV, while that of (0 0 1) is 5.501 eV. The surface energies of (1 1 0) and (1 1 1) planes are quite similar and consistent with the law mentioned above deduced from Fig. 12, which are also helpful to understand the experimental results.

3.3 Application of the theory on the growth process of TiAlSi

As discussed above, by calculating the atomic arrangements on special planes of ZrAlSi phases, we have concluded the growth mechanisms. In order to verify this theory, we also conducted some work on the growth process of TiAlSi. As presented in our previous work [10], there also exists an evolution of TiAlSi phase with the increase of Si content in ternary Al–Si–Ti alloys. Similar with the condition in Al–(Si–)Zr system, the phases can be marked as $TiAl_3$, $Ti(Al_{1-x}Si_x)_3$, and $Ti_7Al_5Si_{12}$, respectively. Here, the chemical $Ti(Al_{1-x}Si_x)_3$ means that some Si atoms replace the sites of Al in the crystal lattice. However, the $Ti(Al_{1-x}Si_x)_3$ phase has the same crystal structure with $TiAl_3$, quite different from the relationship between $Zr(Al_{1-x}Si_x)_3$ ((Al,Zr,Si)) and $ZrAl_3$. Fig. 13 shows the XRD patterns of Al–5Ti, Al–10Si–5Ti and Al–25Si–5Ti alloys. It can be found that the main intermetallic phase in Al–5Ti, Al–10Si–5Ti alloys keeps the crystal structure of $TiAl_3$ (Space Group: I4/mmm; a=0.3844nm, c=0.8596nm; PDF No. 139), while the introduction of Si in $TiAl_3$ leads to an obvious peak shift, as shown in Fig. 13a–b. Since the crystal structure of $TiAl_3$ phase belongs to tetragonal system, the lattice parameters a and c can be calculated using following formula,

$$d = \frac{1}{\sqrt{\frac{h^2 + k^2}{a^2} + \frac{l^2}{c^2}}} \qquad (2)$$

where d is the interplanar spacing, h, k and l are indices of crystallographic planes. Using the values of h, k, l and d corresponding to $Ti(Al_{1-x}Si_x)_3$ diffraction peaks, *e.g.*, $(h_1\ k_1\ l_1) = (1\ 1\ 2)$, d_1

= 2.2806 and (h_2 k_2 l_2) = (0 0 4), d_2 = 2.1464 (Fig. 13b), the parameters *a* and *c* can be obtained, which are 0.3807 nm and 0.8586 nm, respectively. Thus, the replacement of Al atom by Si atom in the $TiAl_3$ crystal lattice leads to the decrease of lattice parameters, since the radius of Si atom is smaller than that of Al atom. Fig. 13c shows the main diffraction peaks of $Ti_7Al_5Si_{12}$ phase (Space Group: $I4_1/amd$; *a*=0.3576nm, *c*=2.715nm; PDF No. 141), which can also be referred as τ_1 in some papers [37]. This crystal structure is quite different from that of $TiAl_3$ or $Ti(Al_{1-x}Si_x)_3$.

Fig. 14 presents the atomic arrangements in the crystal lattices of the three TiAlSi phases. It can be found that Fig. 14a–b confirms the above XRD result, *i.e.* $TiAl_3$ and $Ti(Al_{1-x}Si_x)_3$ has similar crystal structure and diffraction peaks. Correspondingly, the atomic distributions on (0 0 1) (1 1 0) and (1 1 1) faces of $TiAl_3$ and $Ti(Al_{1-x}Si_x)_3$ are the same, just as displayed in Fig. 4a–c. Based on this analysis, it is reasonable to deduce that the growth process and perfect morphologies of TiAlSi particles in Al–5Ti and Al–10Si–5Ti alloys may be similar.

Fig. 15 shows the morphologies of the three Ti–containing phases. Fig. 15a displays the perfect shape of $TiAl_3$, which is quite similar with $ZrAl_3$, *i.e.* both of them present compressed cubic. Fig. 15b and c are the morphologies of $Ti(Al_{1-x}Si_x)_3$ phase. It can be found that, during the growth process, unlike that of $Zr(Al_{1-x}Si_x)_3$, in which four planes perpendicular to the upper and lower surfaces form (Fig. 9b), there appears no such faces. However, it follows the growth mechanism of $TiAl_3$ and $ZrAl_3$, that is to say, the competition between lateral (1 1 0) and (1 1 1) surfaces results in the disappearance of (1 1 1) planes, thus, finally $Ti(Al_{1-x}Si_x)_3$ phase also develops into similar shape with $TiAl_3$. The growth process and mechanism also confirm the theory above, which can be concluded from the atomic arrangements on special crystal planes. Also, the introduction of Si in $TiAl_3$ phase make the compressed cubic much thick (Fig. 15c), similar with the perfect

morphology of $Zr(Al_{1-x}Si_x)_3$.

Fig. 15 d and e show the morphologies of $Ti_7Al_5Si_{12}$. Also, the growth mechanism follows similar process with that of $ZrSi_2$. The initial growing stage is also compressed cubic, whose lateral planes are covered by eight groups of faces. Finally, the faster growing rate along the direction of <0 0 1> results in the formation of 18–polyhedron crystal.

4. Conclusions

The growth mechanism and final morphologies of ZrAlSi phases, *i.e.* $ZrAl_3$, (Al,Zr,Si) and $ZrSi_2$ are discussed in this paper and following conclusions can be obtained:

$ZrAl_3$ phase tends to form compressed cubic, whose upper and lower surfaces are covered by (0 0 1) planes. The growth rate along <0 0 1> is quite slow, resulting in the oblate shape. The lateral surfaces of the compressed cube are four groups of symmetric oblique {1 1 0} surfaces. The higher growth rate of <1 1 0> than <1 1 1> direction leads to the disappearance of {1 1 1} planes.

The perfect (Al,Zr,Si) crystal is similar with that of $ZrAl_3$, and its lateral surfaces are also covered by symmetric {1 1 0} surfaces. However, their growth process is quite different. During the growth stage, (1 0 1), (1 0 $\bar{1}$), (0 1 1), (0 1 $\bar{1}$), ($\bar{1}$ 0 1), ($\bar{1}$ 0 $\bar{1}$), (0 $\bar{1}$ 1) and (0 $\bar{1}$ $\bar{1}$) planes appear on the lateral surfaces of the cube, while (1 1 0), (1 $\bar{1}$ 0), ($\bar{1}$ 1 0) and ($\bar{1}$ $\bar{1}$ 0) planes, perpendicular to the upper and lower (0 0 1) surfaces, also form. Finally, the cube is much thicker than $ZrAl_3$ crystal, due to the higher growth rate along <0 0 1> direction.

The upper and lower surfaces of $ZrSi_2$ phase are also (0 0 1), while the lateral surfaces are covered by eight groups of symmetric {1 1 0} and {1 1 1} planes. The growth rate along <0 0 1> is much faster, resulting in bigger height of the 18–polyhedron than $ZrAl_3$ and (Al,Zr,Si).

The growth process and mechanism of the above Zr–containing phases can be explained

according to the atomic distributions on special crystal planes, which have also been confirmed in Ti–containing phases.

Acknowledgements

The authors wish to thank the financial support of the National Natural Science Foundation of China (No.51271101) and the National Basic Research Program of China (973 Program, No.2012CB825702).

References:

[1] N.A. Belov, D.G. Eskin, N.N. Avxentieva, Acta Mater. 53 (2005) 4709.

[2] L. Lasa, J.M. Rodriguez–Ibabe, J. Mater. Charact. 48 (2002) 371.

[3] X.F. Liu, J.G. Qiao, Y.Y. Wu, X.J. Liu, X.F. Bian, J. Alloys Compd. 388 (2005) 83.

[4] D. Srinivasan, K. Chattopadhyay, Mater. Sci. Eng. A 375 (2004) 1228.

[5] R. Ghomashchi, J. Alloys Compd. 537 (2012) 255.

[6] M. Zeren, E. Karakulak, J. Alloys Compd. 450 (2008) 255.

[7] C. B. Fuller, D.N. Seidman, Acta Mater. 53 (2005) 5401.

[8] O. Schob, H. Nowotny, F. Benesovsky, Planseeber. Pulvermetall. 10 (1962) 65.

[9] T. Hirano, H. Ohtani, M. Hasebe, High Temp. Mater. Processes 29 (2010) 347.

[10] T. Gao, P.T. Li, Y.G. Li, X.F. Liu, J. Alloys Compd. 509 (2011) 8013.

[11] T. Gao, D.K. Li, Z.S. Wei, X.F. Liu, Mater. Sci. Eng. A 552 (2012) 523.

[12] L.F. Mondolfo. Aluminium Alloys: Structure and Properties. Butterworths: London; 1976.

[13] X.G. Chen, M.Fortier, J. Mater. Process Technol. 210 (2010) 1780.

[14] T. Gao, X.F. Liu, J. Mater. Sci. Technol. 29 (2013) 291.

[15] S. Gupta, Mater. Charact. 49 (2003) 321.

[16] L. Arnberg, L. Beckrud, H. Klang, Metals Technol. 9 (1982) 7.

[17] T. Gao, X.Z. Zhu, Q.Q. Sun, X.F. Liu. J. Alloys Compd. 567 (2013) 82.

[18] S. Zhen, G.J. Davies, J. Cryst. Growth 64 (1983) 407.

[19] L. Li, Y.D. Zhang, C. Esling, H.X. Jiang, Z.H. Zhao, Y.B.Zuo, J.Z. Cui, J. Cryst. Growth 316 (2011) 172.

[20] P. Hohenberg, W. Kohn, Phys. Rev. B 136 (1964) 864.

[21] J.F. Janak, L. Morruzi, A.R. Williams, Phys. Rev. B 12 (1975) 1257.

[22] R.J. Kematick, H.F. Franzen, J. Solid State Chem. 54 (1984) 226.

[23] A. Raman, K. Schubert, Z. Metallkund. 56 (1965) 44.

[24] V.P. Kopylova, T.N. Nasarchuk, Ind. Lab. 43 (1977) 485.

[25] K.C. Zhang, L.H. Zhang, Crystal Growth, China Science Press: Beijing, 1981.

[26] G.H. Liu, K.X. Chen, H.P. Zhou, J.J. Tian, C. Pereira, J.M.F. Ferreira, Cryst. Growth Des. 6 (2006) 2404.

[27] P. Hartman, Crystal growth: an introduction. Amsterdam: North– Holland; 1973.

[28] J.W. Gibbs, On the equilibrium of heterogeneous substances, in The Scientific Papers of J. W. Gibbs, 1, Longmans, Green & Co., London; 1906.

[29] P. Curie, J. Chem. Edcn. 47 (1970) 636.

[30] G. Wulff, Z. Krist. 34 (1901) 449.

[31] C. Li, Y.Y. Wu, H. Li, X.F. Liu, Acta Mater. 59 (2011) 1058.

[32] P.T. Li, C. Li, J.F. Nie, J. Ouyang, X.F. Liu, CrystEngComm 15 (2013) 411.

[33] W.M. Wang, X.F. Bian, J.Y. Qin, S.I. Syliusarenko, Met. Mater. Trans. A 31 (2000) 2163.

[34] B.H. Yu, D. Chen, Q.B. Tang, C.L. Wang, D.H. Shi, J Phys. Chem. Solids 71 (2010) 758.

[35] R. Saravanan, M. Charles Robert, J. Alloys Compd. 479 (2009) 26.

[36] M.J. Singh, J. Mater. Sci. 8 (1973) 317.

[37] P. Perrot, Aluminium–silicon–titanium, in: Petzow, G., Effenberg, G. (Eds.), Ternary Alloys–A Comprehensive Compendium of Evaluated Constitutional Data and Phase Diagrams, vol. 8. VCH Publishers, New York, 1990.

Figure Captions

Fig. 1 XRD patterns of Al–5Zr (a), Al–10Si–5Zr (b) and Al–25Si–5Zr (c) alloys.

Fig. 2 Crystal structures of the three Zr–containing phases: (a) $ZrAl_3$, (b) (Al,Zr,Si), (c) $ZrSi_2$.

Fig. 3 Microstructure of Al–5Zr alloy (a), the three–dimensional morphology of $ZrAl_3$ (b), and the corresponding EDS result (c).

Fig. 4 Atomic distributions of (1 0 0) (a), (1 1 0) (b) and (1 1 1) (c) planes, showing the top view and side view, respectively.

Fig. 5 Calculated energies of the model of $ZrAl_3$ containing 48 Al atoms and 16 Zr atoms, with or without vacuum slab: (a) initial model without vacuum slab; (b) with vacuum slab among (0 0 1) planes; (c) with vacuum slab among (1 1 0) planes; (d) with vacuum slab among (1 1 1) planes.

Fig. 6 (a)–(b): Typical morphologies of $ZrAl_3$ at different growth stages. (c)–(d): Scheme of the growth pattern of compressed cube.

Fig. 7 Microstructure of Al–10Si–5Zr alloy (a), the three–dimensional morphology of (Al,Zr,Si) observed in fractograph (b), and the corresponding EDS result (c).

Fig. 8 Atomic distributions of (1 0 0) (a), (1 1 0) (b), (0 1 1) (c) and (1 1 1) (d) planes, showing the top view and side view, respectively.

Fig. 9 (a)–(d): Typical morphologies of (Al,Zr,Si) at different growth stages. (e)–(h): Scheme of the growth pattern.

Fig. 10 Microstructure of Al–25Si–5Zr alloy and EDS analysis of $ZrSi_2$: (a)–(b), polished and deep etched samples, showing the outlines of the particles in two–dimensional observation; (c) the three–dimensional morphology of $ZrSi_2$; (d) the corresponding EDS result.

Fig. 11 (a)–(c): Typical morphologies of $ZrSi_2$. (d)–(e): Scheme of the growth pattern of the 18–polyhedron.

Fig. 12 Atomic distributions of (1 1 0) (a) and (1 1 1) (b) planes, showing the top view and side view, respectively.

Fig. 13 XRD patterns of Al–5Ti (a), Al–10Si–5Ti (b) and Al–25Si–5Ti (c) alloys.

Fig. 14 Crystal structures of the three Ti–containing phases: (a) $TiAl_3$, (b) Ti $(Al_{1-x}Si_x)_3$, (c) $Ti_7Al_5Si_{12}$.

Fig. 15 Morphologies of $TiAl_3$ (a), Ti $(Al_{1-x}Si_x)_3$ (b, c) and $Ti_7Al_5Si_{12}$ (d, e) phases.

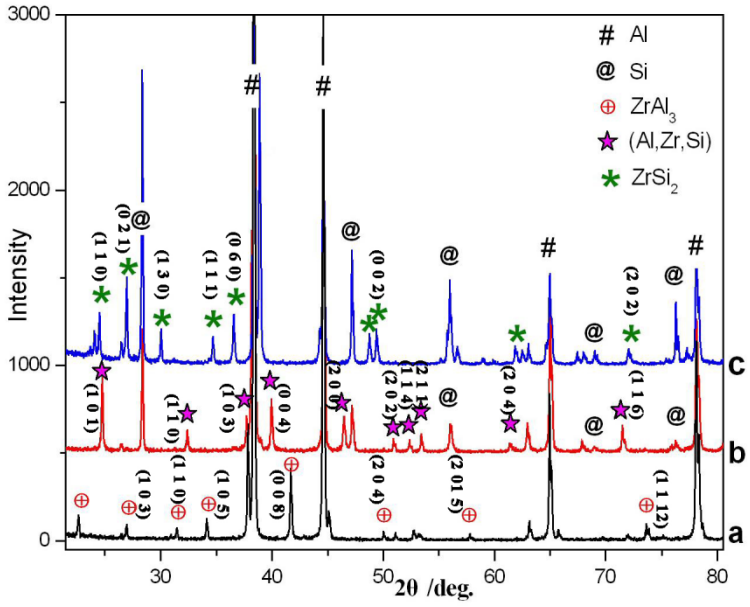

Fig. 1

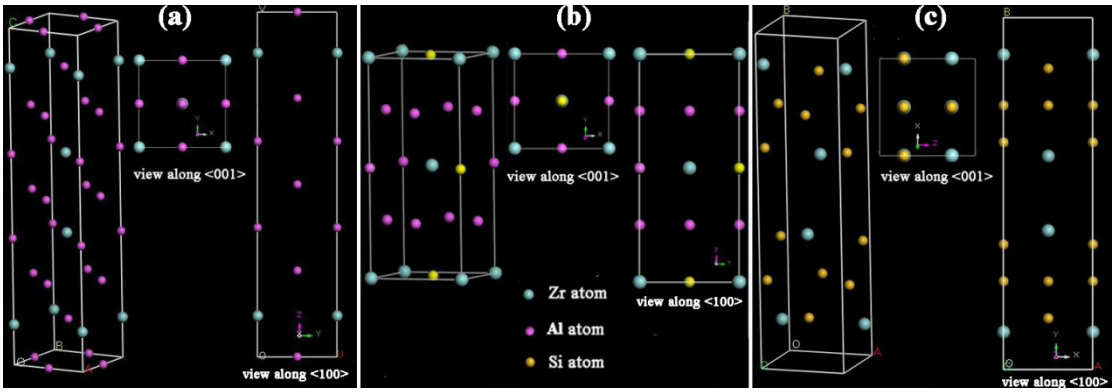

Fig. 2

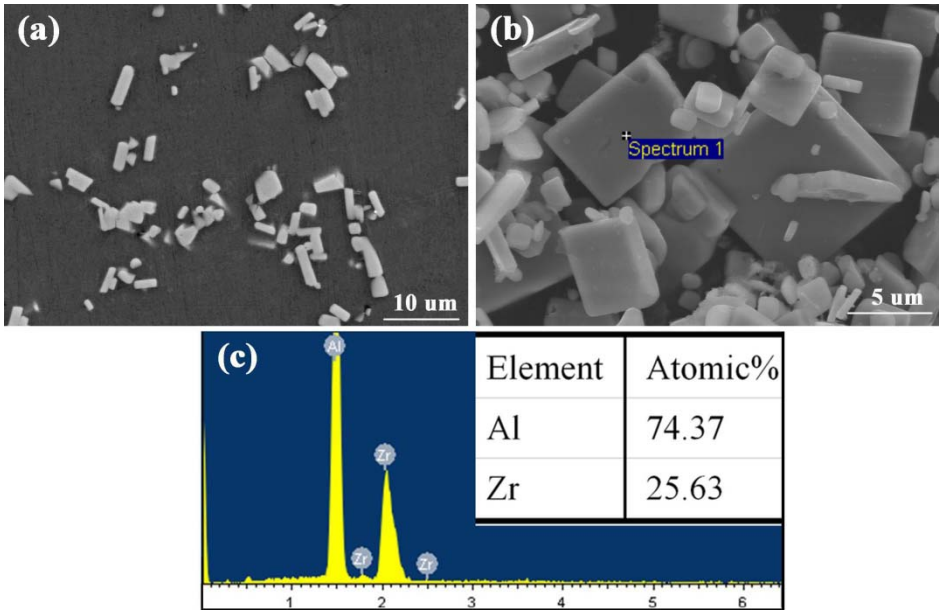

Fig. 3

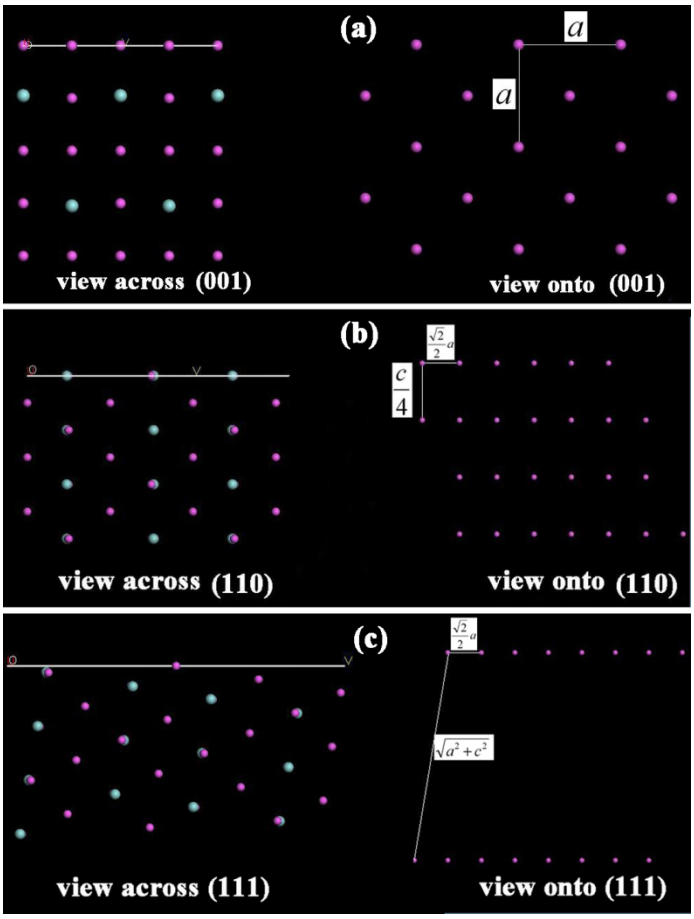

Fig. 4

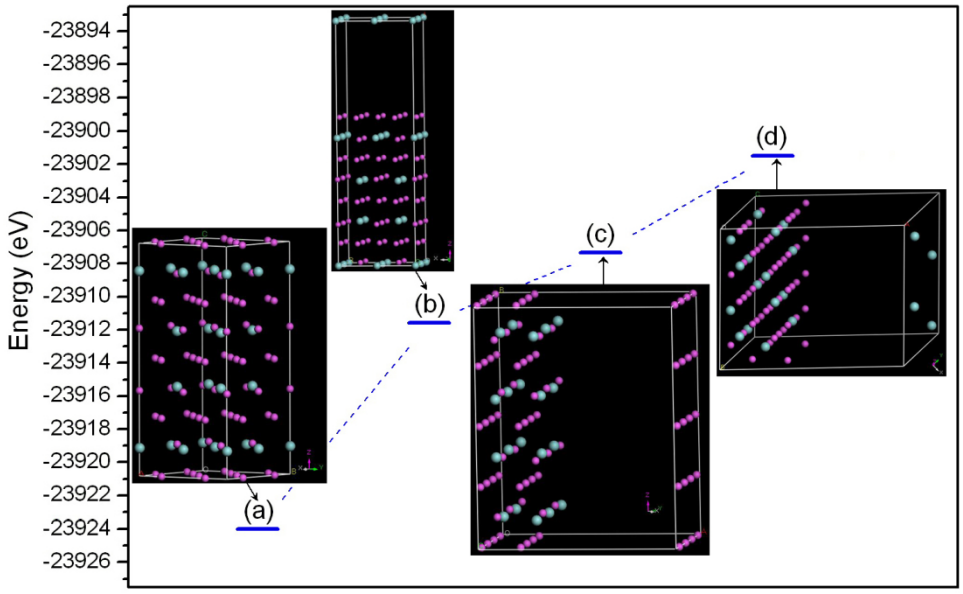

Fig. 5

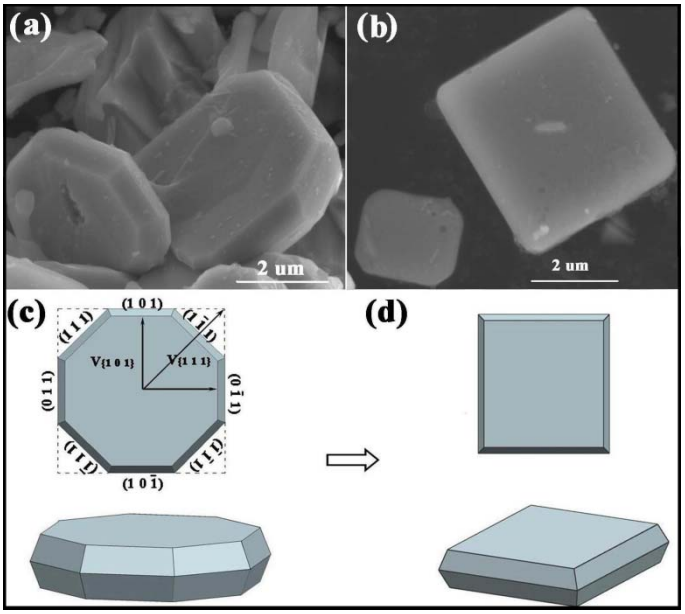

Fig. 6

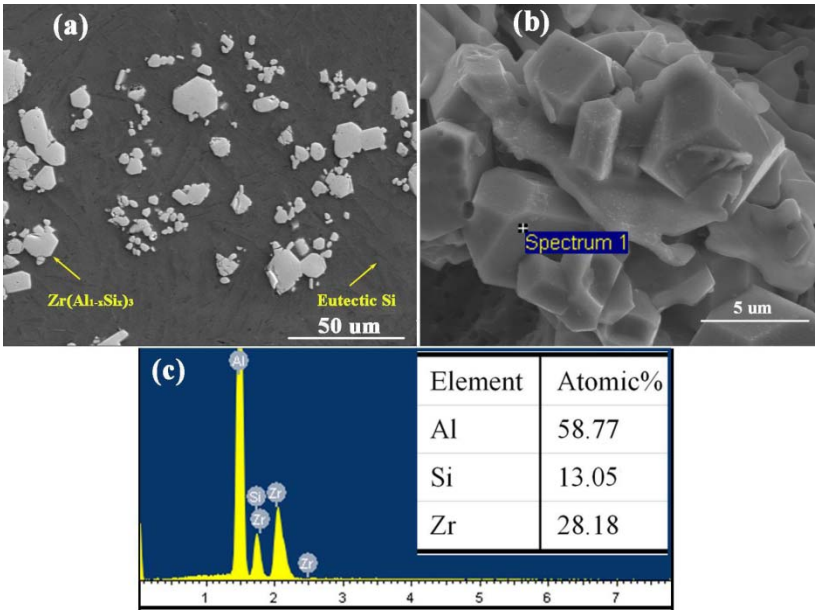

Fig. 7

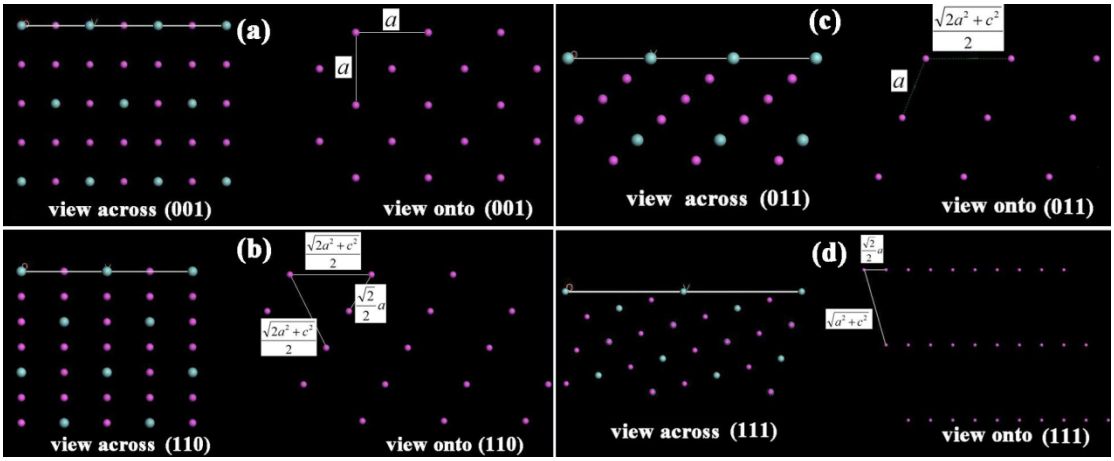

Fig. 8

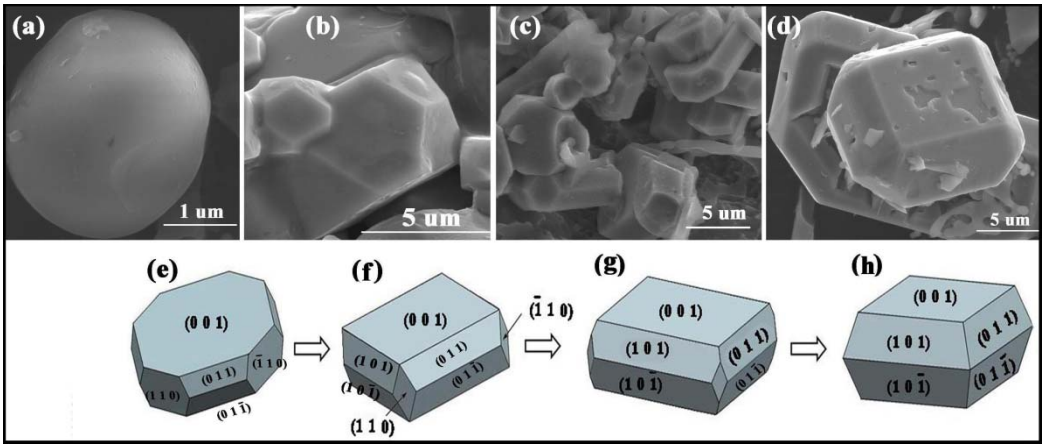

Fig. 9

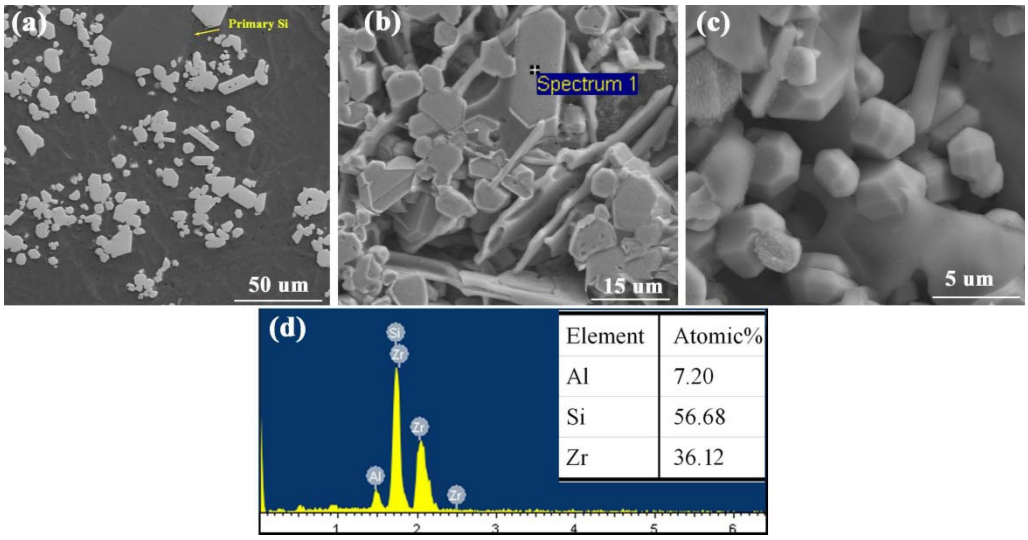

Fig. 10

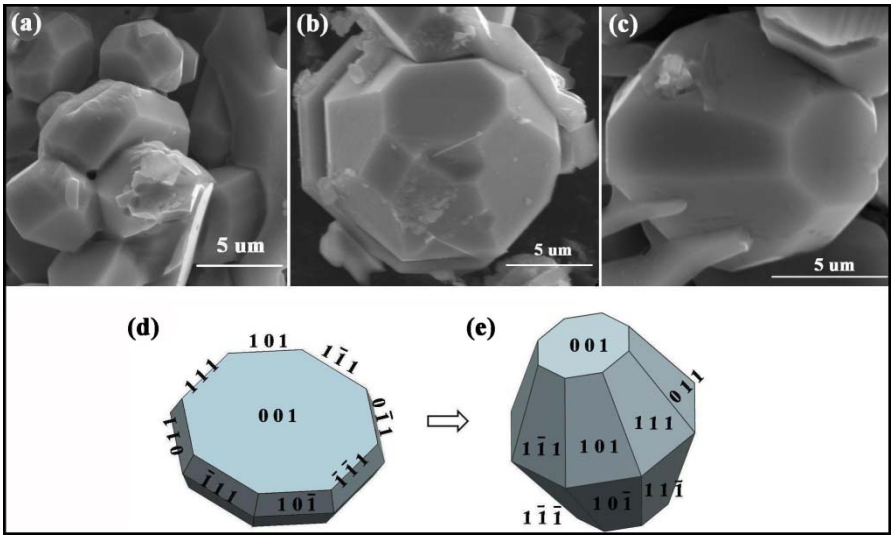

Fig. 11

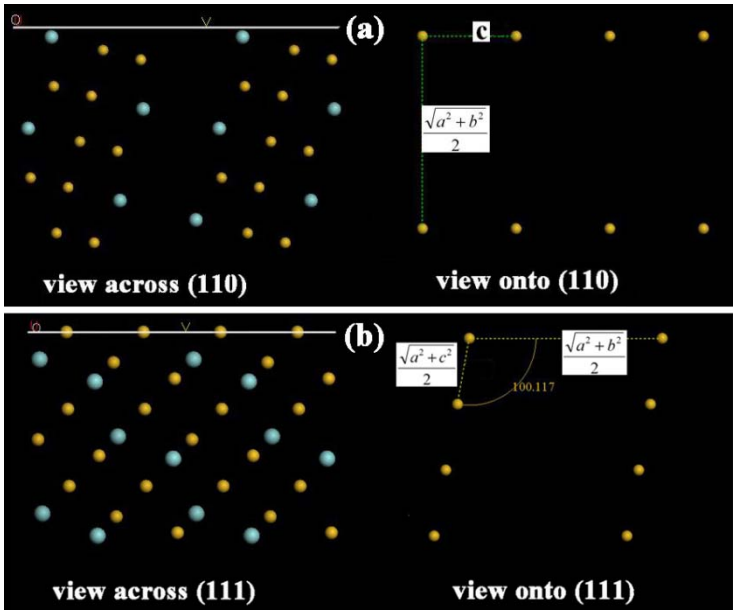

Fig. 12

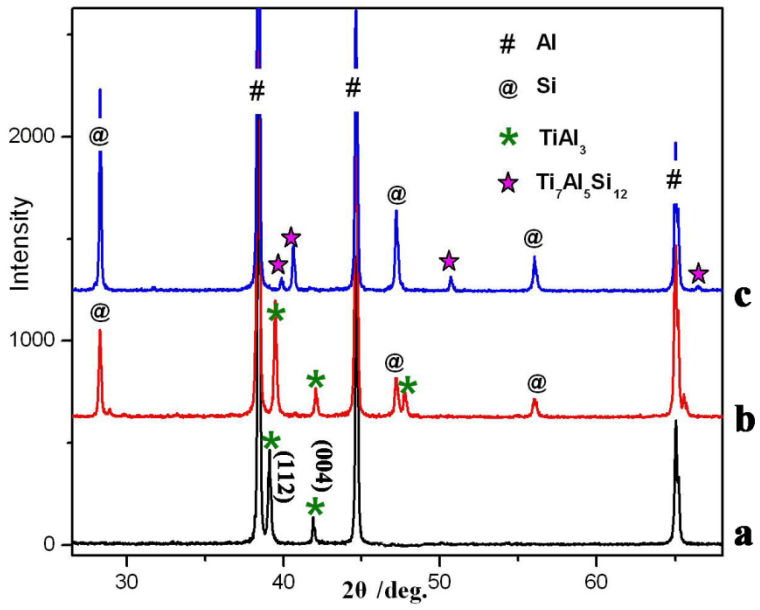

Fig. 13

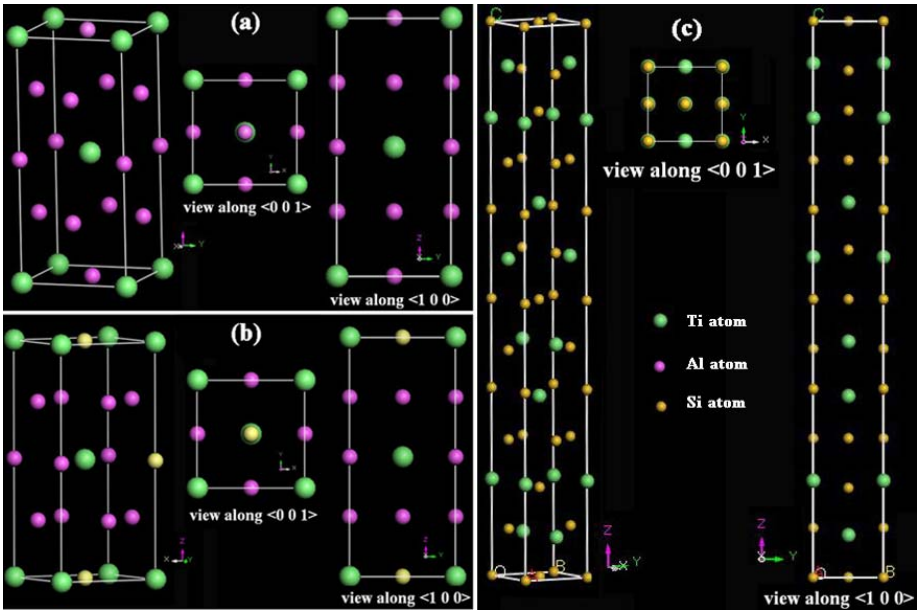

Fig. 14

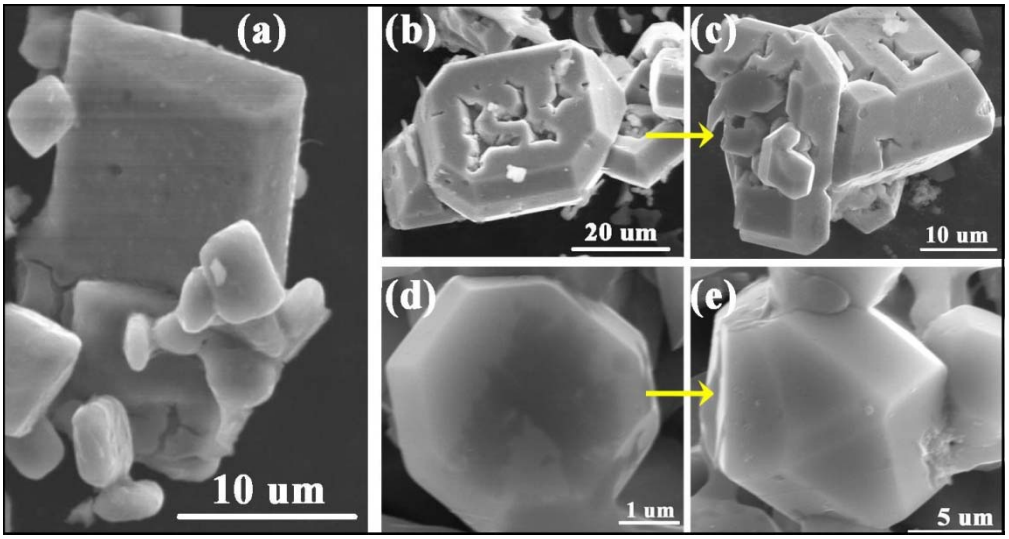

Fig. 15

Graphical Abstract

Increase of Si in Al–Si–Zr alloys causes evolutions of structures, morphologies and growth patterns of Zr–containing phases.